Interparticle normal force in highly porous granular matter during compression

Sota Arakawa [1,*] Misako Tatsuuma [2,3] Hidekazu Tanaka [4] Mikito Furuichi [1] and Daisuke Nishiura [1]

[1]*Yokohama Institute for Earth Sciences, Japan Agency for Marine-Earth Science and Technology, 3173-25, Showa-machi, Kanazawa-ku, Yokohama 236-0001, Japan*

[2]*RIKEN Interdisciplinary Theoretical and Mathematical Sciences Program (iTHEMS), 2-1 Hirosawa, Wako, Saitama 351-0198, Japan*

[3]*Department of Earth and Planetary Sciences, Tokyo Institute of Technology, 2-12-1 Ookayama, Meguro, Tokyo 152-8550, Japan*

[4]*Astronomical Institute, Graduate School of Science, Tohoku University, 6-3 Aramaki, Aoba-ku, Sendai 980-8578, Japan*

(Received 19 July 2023; accepted 24 January 2024; published 27 February 2024)

We perform a numerical simulation of compression of a highly porous dust aggregate of monodisperse spheres. We find that the average interparticle normal force within the aggregate is inversely proportional to both the filling factor and the average coordination number and we also derive this relation theoretically. Our findings would be applicable for granular matter of arbitrary structures, as long as the constituent particles are monodisperse spheres.

DOI: 10.1103/PhysRevE.109.024904

I. INTRODUCTION

Granular materials are ubiquitous on earth and in space [1–5] and understanding their physical properties is of great importance in various fields of science and engineering [6–8]. Granular materials have been usually defined as agglomerates of discrete particles and the interparticle contact area is a function of the normal force acting between two contact particles [9–11]. The interparticle contact area is a key parameter which controls thermal and mechanical properties of granular matter [12–16]. In addition, constituent particles would be broken when the interparticle force exceeds the threshold for failure [17–19]. Therefore, the interparticle force in compressed granular matter has been intensively investigated [20–22].

When constituent particles have large static frictions for tangential motions, highly porous structure would be achieved by compression with low pressure [23–25]. Indeed, highly porous dust aggregates with filling factors below 10% might exist in protoplanetary disks as building blocks of planets [26–30]. In disks, such porous aggregates could be formed via pairwise collisional growth [31–33] and the initial structure of those aggregates would resemble that of fractal aggregates formed by the ballistic cluster-cluster aggregation process [34].

However, the interparticle force in compressed fluffy aggregates has never been investigated. This is because preparation of initial fractal aggregates in laboratories is difficult in nonzero gravity conditions [35]. The measurement of interparticle force is also challenging when the force is small. In contrast, numerical simulations are not affected by those difficulties and we can investigate how the interparticle force changes with increasing the filling factor of porous aggregates.

In this study, we perform a three-dimensional numerical simulation using the soft-sphere discrete element method and demonstrate the temporal evolution of the interparticle force during omnidirectional compression. As a consequence, we find that the average interparticle normal force, $\langle F \rangle$, is given by a simple function of the pressure, P, the filling factor, ϕ, and the average coordination number, $\langle Z \rangle$. We also reveal that this relation is directly derived from the definition of the pressure in granular matter. Our findings would be widely applicable when we evaluate the thermal or mechanical properties of fluffy aggregates.

II. NUMERICAL METHOD

We perform a numerical simulation of compression of a highly porous dust aggregate of monodisperse spheres. The number of particles in the simulation is $N = 2^{14} = 16\,384$ and the constituent dust particles are made of water ice whose radius is $r_1 = 0.1\,\mu\text{m}$. The material properties including the elastic modulus and the surface energy are summarized in Ref. [36]. The numerical code used in this study is identical to that of previous studies [37,38]. We calculate the translational and rotational motions of each particle by solving the Newton-Euler equations. We integrate these equations using the leapfrog method, which is a second-order symplectic integrator with a good accuracy of energy conservation.

In this study, we assume that the interparticle normal motion is described by a contact model for elastic cohesive spheres called the JKR model [10]. The interparticle normal force, F, is a function of the compression length between two contact particles, δ. We define δ as

$$\delta = 2r_1 - d \tag{1}$$

and d is the distance between the two particles' centers. Two contact particles make a circular contact area and the contact radius, a, is also a function of δ.

*arakawas@jamstec.go.jp

At the equilibrium state where $F = 0$, the contact radius is $a = a_0$ and the compression length is $\delta = \delta_0$. Here a_0 is given by

$$a_0 = \left(\frac{9\pi\gamma R^2}{E^*}\right)^{1/3} = 12.4\ \text{nm}, \tag{2}$$

where $\gamma = 0.1\ \text{J m}^{-2}$ [36] is the surface energy, E^* is the reduced Young's modulus, and R is the reduced particle radius [10]. In this study, we assume that the two contact particles have the same radius and composition and R and E^* are given by

$$R = \frac{r_1}{2} \tag{3}$$

and

$$E^* = \frac{E}{2(1-\nu^2)}, \tag{4}$$

where $E = 7$ GPa is Young's modulus and $\nu = 0.25$ is Poisson's ratio [36]. The compression length at the equilibrium is

$$\delta_0 = \frac{{a_0}^2}{3R} \tag{5}$$

and $\delta_0 = 1.0$ nm for $r_1 = 0.1$ μm.

Here we introduce the normalized compression length, x, as follows:

$$x = \frac{\delta}{\delta_0}. \tag{6}$$

We also introduce a dimensionless function, y, which describes the contact radius:

$$y = \left(\frac{a}{a_0}\right)^{1/2}. \tag{7}$$

The relation between x and y is given by Ref. [10] as follows:

$$3y^4 - 2y - x = 0. \tag{8}$$

We also derive an equivalent equation which explicitly expresses y as a function of x as follows:

$$y = \frac{1}{2}\left(-A(x) + \frac{4}{3\sqrt{A(x)}}\right)^{1/2} + \frac{\sqrt{A(x)}}{2}, \tag{9}$$

where $A(x)$ is given by

$$A(x) = \frac{2^{1/3}\alpha(x)}{3} - \frac{2^{5/3}x}{3\alpha(x)} \tag{10}$$

and $\alpha(x)$ is

$$\alpha(x) = \left(\sqrt{16x^3 + 9} + 3\right)^{1/3}. \tag{11}$$

This is one of the real solutions of Eq. (8). The interparticle contact breaks at $x = -(9/16)^{1/3}$ and $y = (1/6)^{1/3}$ at the time. For the JKR model, y is a monotonically increasing function of x. The explicit formulation derived here is useful when we calculate y as a function of x [39].

We also define the normalized force acting between two contact particles, z, as follows [10]:

$$z = \frac{F}{F_c}, \tag{12}$$

where F_c is the maximum force needed to disconnect the two contact particles. In the contact model of Ref. [10], F_c is given by

$$F_c = 3\pi\gamma R \tag{13}$$

and $F_c = 4.7 \times 10^{-8}$ N for $r_1 = 0.1$ μm. The relation between y and z is given by [10,36]

$$z = 4(y^6 - y^3). \tag{14}$$

By solving these equations, we can calculate z as a function of x. In other words, F is given as a function of δ. We note that F is positive when the repulsive force acts on two contact particles.

The elastic force in the normal direction induces oscillation. However, in reality, the oscillation would be damped due to viscoelastic energy dissipation [40–42]. In our simulation, the damping force applied to each pair of two contact particles is introduced. The detail of damping model is described in Ref. [37] (see Appendix A).

The interparticle tangential interactions are modeled by Ref. [36]. We consider three types of motions: rolling, sliding, and twisting. When the displacements are small, the resistances against these displacements are described by elastic spring models, while inelastic motions take place when the displacements exceed the critical values (see Figs. 2 and 3 of Ref. [36]). The detail of particle interaction models is described in Ref. [36] (see Appendix B).

We prepare an initial dust aggregate by ballistic cluster-cluster aggregation as in previous studies [24,37,38]. Then we perform an isotropic compression simulation as investigated by Refs. [24,38]. We adopt the periodic boundary condition (Fig. 1) and a cubic box with a volume of L^3 is considered as the computational region. The box size decreases with time, t, as follows:

$$\frac{dL}{dt} = -\frac{2C_v L}{t_c}, \tag{15}$$

where $C_v = 1 \times 10^{-7}$ is the strain rate parameter [24] and $t_c = 1.93 \times 10^{-10}$ s is the characteristic time of interparticle normal interaction [36]. The volume filling factor at each time step is defined as follows:

$$\phi = \frac{4\pi {r_1}^3 N}{3L^3}. \tag{16}$$

III. RESULTS AND DISCUSSION

First, we show the frequency distribution of interparticle normal force during compression [43]. Figure 2 shows the cumulative frequency distribution of F within an aggregate. Here $f_{\text{cum}}(< F)$ is the fraction of particle connections whose normal force is smaller than F. The differential frequency distribution of F is shown in Appendix C as a reference.

We can see a jump of $f_{\text{cum}}(< F)$ at around $F = 0$ in Fig. 2(a) and a large fraction of particle connections is piled up at $F \approx 0$ when $\phi \leqslant 0.1$. In contrast, no strong pileup at $F \approx 0$ is observed for $\phi = 0.25$ [Fig. 2(b)]. This result reflects the change of particle chain structures within the aggregate: a large fraction of particles in highly porous aggregates are not in backbone structure but in noncontributing deadends (see also Fig. 6 of Ref. [44]).

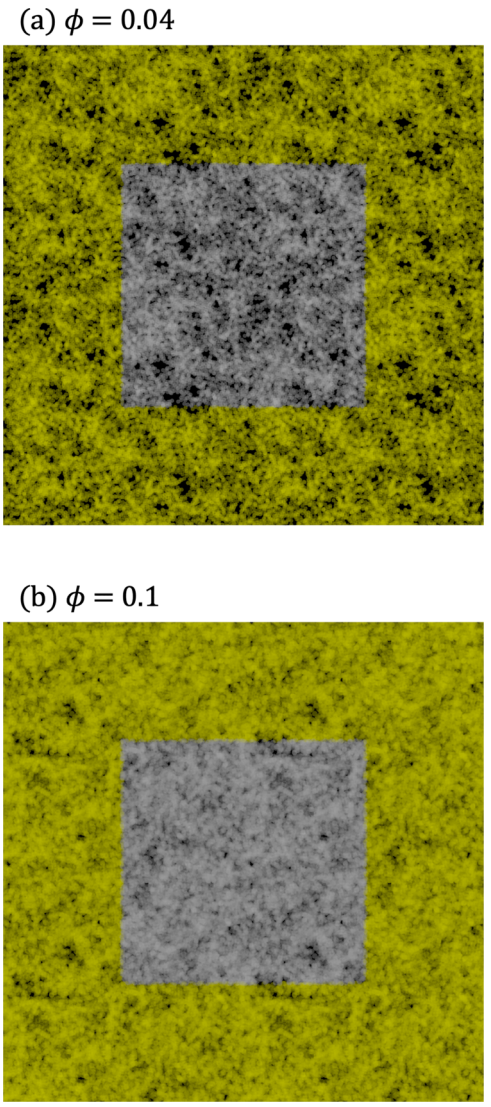

FIG. 1. Snapshots of the structure evolution of an aggregate during compression in a cubic periodic boundary. The gray particles are inside a cubic box. We also plot the yellow particles which are in neighboring boxes to the box of gray particles. The box size decreases with time and the filling factor, ϕ, increases with time. Panels (a) and (b) are the snapshots at $\phi = 0.04$ and 0.1, respectively. The length of the box is $L = 119.9r_1$ for panel (a) and $L = 88.2r_1$ for panel (b).

We investigate the dependence on the compression speed (C_v) and damping force (k_n) in Appendix D. We confirm that the distribution of $f_{cum}(< F)$ barely depends on C_v and k_n.

Next, we show the average of the interparticle normal force, $\langle F \rangle$, and its dependence on the filling factor. Figure 3 shows $\langle F \rangle$ as a function of ϕ. We find that $\langle F \rangle$ increases with ϕ during compression and for $\phi \leqslant 0.25$ we find $\langle F \rangle / F_c \ll 1$, which allows us to consider the compression length to be constant, $\delta \approx \delta_0$. We note that $\langle F \rangle / F_c$ also depends on the material properties and radius of constituent particles and this result is only applicable for aggregates made of water ice particles with $r_1 = 0.1$ μm.

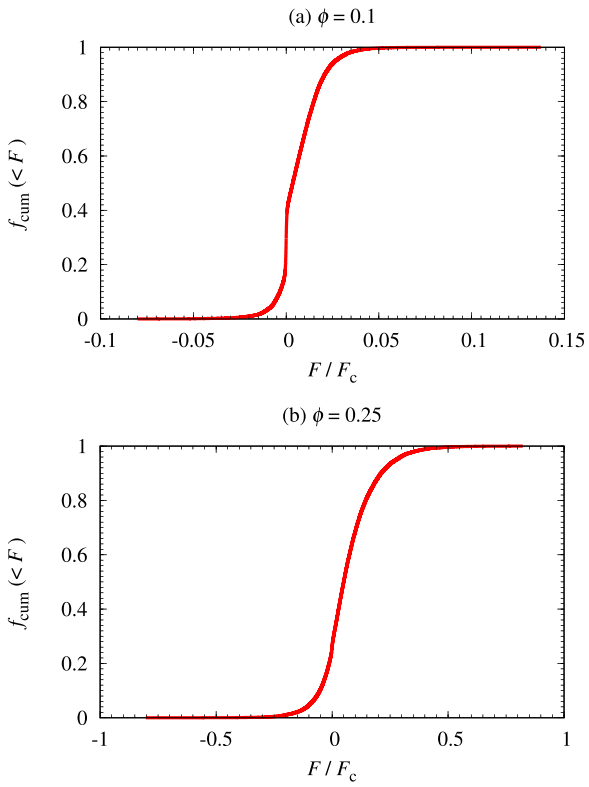

FIG. 2. Cumulative frequency distribution of interparticle normal force. Here $f_{cum}(< F)$ is the fraction of particle connections whose normal force is smaller than F. The compression length between contacting particles is $\delta = \delta_0$ when $F = 0$. Panels (a) and (b) are for the cases of $\phi = 0.1$ and 0.25, respectively.

Finally, we discuss the relation between $\langle F \rangle$ and the pressure of the dust aggregate, P. In this study, an aggregate is compressed by itself as we use the periodic boundary condition. The pressure of the aggregate is defined by the standard method in molecular dynamics simulations which is based on the virial theorem [45]. In our numerical simulation, P is

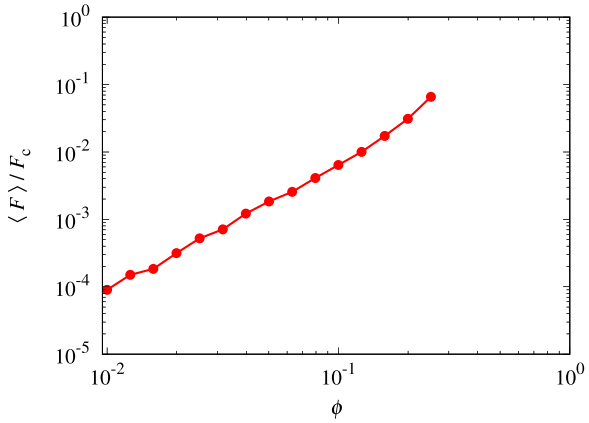

FIG. 3. Average of the interparticle normal force, $\langle F \rangle$, as a function of ϕ. Here we assume that constituent particles are made of water ice and the radius is $r_1 = 0.1$ μm.

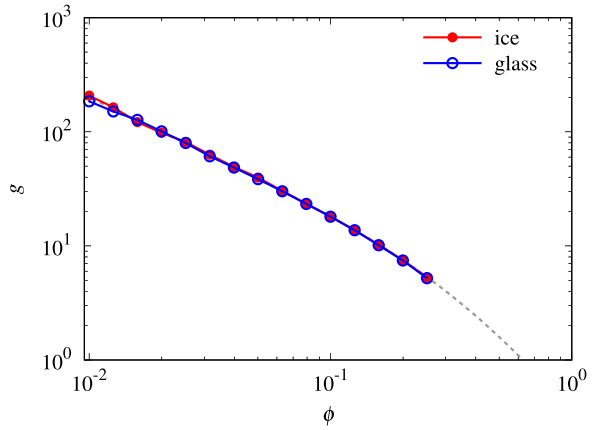

FIG. 4. Normalized normal force, g, as a function of ϕ. The dashed line is a theoretical prediction [Eq. (22)]. Red and blue points denote our numerical result for ice and glass spheres, respectively.

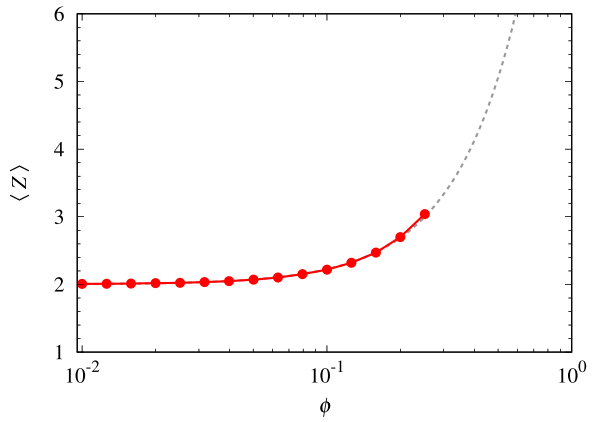

FIG. 5. Average coordination number, $\langle Z\rangle$, as a function of ϕ. The dashed line is a semianalytic model in previous studies: $\langle Z\rangle = 2 + 9.38\phi^{1.62}$ [44,47].

defined as follows [24,46]:

$$P = \left\langle \frac{2}{3L^3}\sum_{i=1}^{N}\frac{mv_i^2}{2} + \frac{1}{3L^3}\sum_{i<j} d_{i,j}F_{i,j}\right\rangle_t, \tag{17}$$

where m is the mass of each particle, v_i is the velocity of the ith particle, $d_{i,j}$ is the distance between the ith and jth particles, and $F_{i,j}$ is the interparticle normal force between ith and jth particles. Assuming that the material density of ice is $\rho = 1000\ \mathrm{kg\,m^{-3}}$ [36], m is given by $m = (4\pi/3)\rho {r_1}^3 = 4.2\times10^{-18}$ kg. Here $F_{i,j}$ is positive when the repulsive force works and $F_{i,j} = 0$ if ith and jth particles do not contact. We calculate the time-averaged value of P and $\langle\mathcal{A}\rangle_t$ denotes the time average of a variable $\mathcal{A}$. We take an average of the right-hand side of Eq. (17) for $10^3 t_c$, which is sufficiently longer than the characteristic time of particle interaction ($= t_c$) and negligibly shorter than the timescale of compression [$= 5\times10^6 t_c$; see Eq. (15)] [24,38].

We introduce the normalized normal force, g, as follows:

$$g = \frac{\langle F\rangle}{\pi {r_1}^2 P}. \tag{18}$$

In our simulation, the porous aggregate is continuously compressed and the applied pressure is balanced with the compressive strength. In contrast, when the applied pressure is lower than the compressive strength and the deformation of an aggregate is negligible, $\langle F\rangle$ must be proportional to P. Thus we can interpret g as a constant of proportionality. The red line of Fig. 4 shows g for the range between $\phi = 0.01$ and 0.25.

It should be noted that g would be independent of the material parameters of the constituent particles. Here we perform an additional simulation using dust aggregates of glass spheres. The material parameters of glass spheres are $\gamma = 0.02\ \mathrm{J\,m^{-2}}$, $E = 54$ GPa, $\nu = 0.17$, and $\rho = 2650\ \mathrm{kg\,m^{-3}}$ [36]. We set $C_v = 3\times10^{-7}$ and $k_n = 0.1$ for this case. The particle radius is set to be equal to that for ice aggregates: $r_1 = 0.1$ μm. The number of constituent particles and the initial structure of the aggregate are also identical to those for ice aggregates. The blue line of Fig. 4 denotes our numerical result for glass spheres. It is obvious that numerical results for both ice and glass aggregates are consistent with each other.

Here we show that g could be derived analytically from the definition of P. When the compression speed is sufficiently low, we can regard the compression as a quasistatic process (i.e., $v_i \approx 0$) and Eq. (17) is approximated by

$$P \approx \frac{1}{3L^3}\sum_{i<j} d_{i,j}F_{i,j}. \tag{19}$$

When $\langle F\rangle/F_c \ll 1$, we can assume that $d_{i,j} \approx 2r_1 - \delta_0$ for all particle connections and we obtain the following equation:

$$\sum_{i<j} d_{i,j}F_{i,j} \approx \frac{2r_1}{c_0}\langle F\rangle N\frac{\langle Z\rangle}{2}, \tag{20}$$

where

$$c_0 = \frac{2r_1}{2r_1 - \delta_0} \tag{21}$$

is a correction factor ($c_0 = 1.005$ for ice particles with $r_1 = 0.1$ μm) and $\langle Z\rangle$ is the average coordination number. Therefore, we derive the following equation:

$$g \approx \frac{4c_0}{\langle Z\rangle\phi} \tag{22}$$

and g is inversely proportional to both ϕ and $\langle Z\rangle$. The dashed line in Fig. 4 is the theoretical prediction and it shows excellent agreement with the numerical result.

The average coordination number should also be a function of ϕ and it must depend on how to prepare the initial aggregate before compression. Figure 5 shows the filling factor dependence of $\langle Z\rangle$. When the initial fluffy aggregates were prepared by the ballistic cluster-cluster aggregation process, the filling factor dependence of $\langle Z\rangle$ is given by [44,47]

$$\langle Z\rangle = 2 + 9.38\phi^{1.62}. \tag{23}$$

We confirm that our numerical result is consistent with a model prediction.

Although the filling factor dependence of g is trivial when we go back to the definition of P in molecular dynamics

simulations, it has been poorly understood. Several predictions on g have been reported; e.g., $g = (2/\sqrt{6})\phi^{-1}$ [15] or $g = \phi^{-1}$ [18]. These studies did not mention the dependence of g on $\langle Z \rangle$, however. When we focus on fluffy aggregates with $\phi \ll 0.1$, we can regard $\langle Z \rangle \approx 2$ and it barely depends on ϕ. In contrast, for $\phi \gtrsim 0.1$, $\langle Z \rangle$ clearly depends on ϕ (Fig. 5) and the effect of $\langle Z \rangle$ on g is non-negligible.

We note that Eq. (22) would be applicable for dust aggregates of arbitrary structures, as long as the constituent particles could be regarded as monodisperse spheres. We expect that $\langle Z \rangle \approx 2$ whenever ϕ is order(s) of magnitude lower than 1, however, the filling factor dependence of $\langle Z \rangle$ is different for each preparation procedure of aggregates [44,48].

It should be noted that not all particles do not contribute heat and pressure transfer within aggregates. As shown in Fig. 2, a substantial fraction of interparticle contacts is force free when $\phi \leqslant 0.1$. We might need to evaluate the effective mean of F by averaging over contacts with nonzero F when the effects on the thermal and mechanical properties of aggregates are considered.

IV. CONCLUSION

Summarizing, the relationship among the pressure within an aggregate, P, the filling factor, ϕ, the average coordination number, $\langle Z \rangle$, and the average interparticle normal force, $\langle F \rangle$, is derived once numerically and then theoretically [Eqs. (18) and (22)]. We found that $\langle F \rangle$ is inversely proportional to both ϕ and $\langle Z \rangle$. The filling factor dependence is consistent with that predicted in previous studies [15,18]. We derived this dependence from the definition of the pressure in granular matter. We also note that g would be independent of the material parameters of the constituent particles (Fig. 4).

Understanding the interparticle normal force and its dependence on the other parameters are essential to predict the thermal and mechanical properties of granular matter. Our findings will provide deeper insight into the physics of porous granular matter. We expect that our theoretical prediction will be tested by laboratory experiments.

Finally, we note that not only the average of F but also the distribution of F is of great interest. The failure of particles under pressure should start when the maximum of F exceeds the threshold and the disruption of constituent particles changes the size distribution of particles. The force chain structure should also be affected by the failure. We will address these issues in future studies.

ACKNOWLEDGMENTS

This work was supported by JSPS KAKENHI Grants No. JP22J00260 and No. JP22KJ1292.

APPENDIX A: DAMPING FORCE FOR INTERPARTICLE NORMAL MOTION

The elastic interparticle normal force, F, induces oscillation at each connection. The oscillation would attenuate in reality due to energy dissipation. In this study, we introduce an artificial damping force in the normal direction which is modeled in Ref. [24]. The damping force applied to each particle is given by

$$F_{\rm damp} = -k_{\rm n}\frac{m}{t_{\rm c}}v_{\rm rel,n}, \tag{A1}$$

where $k_{\rm n}$ is the dimensionless coefficient and $v_{\rm rel,n}$ is the normal component of the relative velocity between two contacting particles. Note that $v_{\rm rel,n}$ is negative when two particles approach. We adopt $k_{\rm n} = 0.01$ as a fiducial value [38].

APPENDIX B: TANGENTIAL INTERACTION MODELS

We calculate the interaction of each connection of particles, taking all interactions modeled by Ref. [36] into account. The mechanical model for the normal interaction is described in Sec. II in detail. Here we briefly explain the models for the tangential interactions.

We consider three types of tangential motions, namely, rolling, sliding, and twisting (see Fig. 2 of Ref. [36]). The displacements corresponding to these motions are expressed by the rotation of the two particles in contact. In the framework of the contact model developed by Ref. [36], the elastic and inelastic regimes are considered for each interaction: no energy is dissipated when the displacements of the tangential motions are all small enough, while energy dissipation occurs when the displacements exceed the threshold values. The forces and torques on each particle due to tangential interactions are originally formulated by Refs. [49,50]. The detail of the interaction models is described in Sec. 2.2 of Ref. [36].

APPENDIX C: DIFFERENTIAL FREQUENCY DISTRIBUTION OF INTERPARTICLE NORMAL FORCE

In the granular community, the frequency distribution of interparticle normal force is usually presented in the differential frequency distribution [20–22]. Although we choose the cumulative distribution instead of the differential one in Sec. III, we present the differential frequency distribution in this Appendix.

Figure 6 shows the differential frequency distribution of interparticle normal force, $p_{\rm diff}(F/F_{\rm c})$, for the case of $\phi = 0.1$ [see Fig. 2(b)]. Here $p_{\rm diff}(F/F_{\rm c})$ is given by

$$p_{\rm diff}(F/F_{\rm c}) = \frac{f_{\rm cum}[< (i+1/2)\Delta F_{\rm c}]}{\Delta} - \frac{f_{\rm cum}[< (i-1/2)\Delta F_{\rm c}]}{\Delta}, \tag{C1}$$

where Δ is the bin width of the differential distribution and $F = i\Delta F_{\rm c}$ ($i = 0, \pm1, \pm2, \ldots$). Panels (a) and (b) are for the cases of $\Delta = 0.01$ and 0.001, respectively. We find that the shape of the distribution is strongly affected by the choice of Δ.

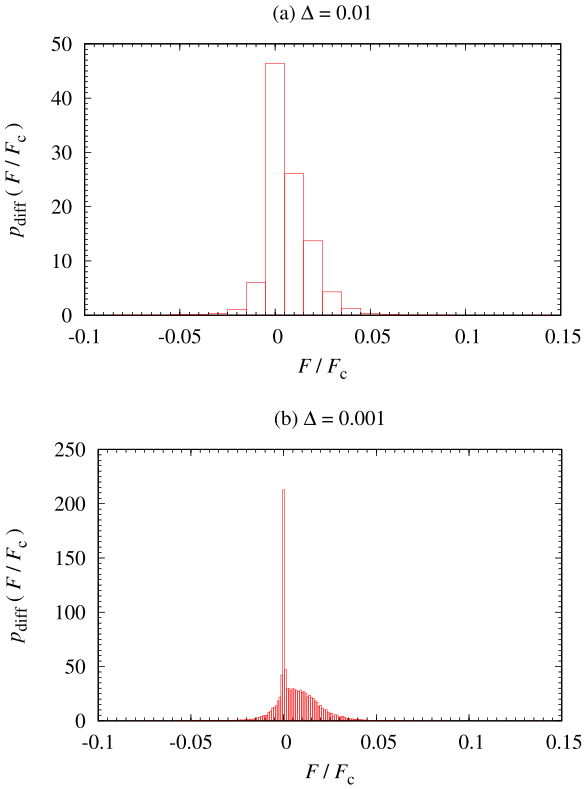

FIG. 6. Differential frequency distribution of interparticle normal force for the case of $\phi = 0.1$ [see Fig. 2(b)]. Panels (a) and (b) are for the cases of $\Delta = 0.01$ and 0.001, respectively.

We can see a clear pileup at $F \approx 0$ in Fig. 6(b), as discussed in Sec. III [see also Fig. 2(b)]. This reflects the fact that a non-negligible fraction of particles in highly porous aggregates are not in backbone structure.

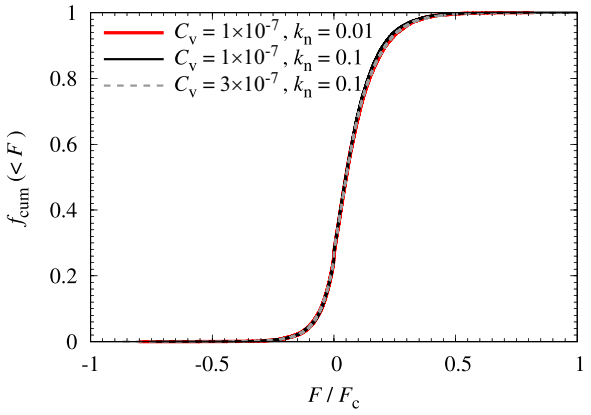

FIG. 7. Cumulative frequency distribution of interparticle normal force, $f_{\rm cum}(< F)$, for $\phi = 0.25$. The red line represents the fiducial case ($C_{\rm v} = 1 \times 10^{-7}$ and $k_{\rm n} = 0.01$). The black line is a strong dissipation case ($C_{\rm v} = 1 \times 10^{-7}$ and $k_{\rm n} = 0.1$). The gray dashed line is a strong dissipation and fast compression case ($C_{\rm v} = 3 \times 10^{-7}$ and $k_{\rm n} = 0.1$).

APPENDIX D: DEPENDENCE ON $C_{\rm v}$ AND $k_{\rm n}$

To check the robustness of our numerical results, we perform additional simulations with different parameter sets of $C_{\rm v}$ and $k_{\rm n}$. Figure 7 shows the cumulative frequency distribution of interparticle normal force, $f_{\rm cum}(< F)$, for $\phi = 0.25$. The red line represents the fiducial case and black and gray dashed lines show the results for different sets of $C_{\rm v}$ and $k_{\rm n}$. We confirm that $f_{\rm cum}(< F)$ is approximately independent of $C_{\rm v}$ and $k_{\rm n}$.

[1] H. M. Jaeger, S. R. Nagel, and R. P. Behringer, Granular solids, liquids, and gases, Rev. Mod. Phys. **68**, 1259 (1996).

[2] R. M. Iverson, M. E. Reid, and R. G. Lahusen, Debris-flow mobilization from landslides, Annu. Rev. Earth Planet Sci. **25**, 85 (1997).

[3] H. Miyamoto, H. Yano, D. J. Scheeres, S. Abe, O. Barnouin-Jha, A. F. Cheng, H. Demura, R. W. Gaskell, N. Hirata, M. Ishiguro, T. Michikami, A. M. Nakamura, R. Nakamura, J. Saito, and S. Sasaki, Regolith migration and sorting on asteroid itokawa, Science **316**, 1011 (2007).

[4] J. Blum and G. Wurm, The growth mechanisms of macroscopic bodies in protoplanetary disks, Annu. Rev. Astron. Astrophys. **46**, 21 (2008).

[5] A. Tsuchiyama, M. Uesugi, T. Matsushima, T. Michikami, T. Kadono, T. Nakamura, K. Uesugi, T. Nakano, S. A. Sandford, R. Noguchi, T. Matsumoto, J. Matsuno, T. Nagano, Y. Imai, A. Takeuchi, Y. Suzuki, T. Ogami, J. Katagiri, M. Ebihara, T. R. Ireland *et al.*, Three-dimensional structure of hayabusa samples: Origin and evolution of itokawa regolith, Science **333**, 1125 (2011).

[6] H. Katsuragi and D. J. Durian, Unified force law for granular impact cratering, Nat. Phys. **3**, 420 (2007).

[7] T. Matsushima, J. Katagiri, K. Uesugi, A. Tsuchiyama, and T. Nakano, 3D shape characterization and image-based DEM simulation of the lunar soil simulant FJS-1, J. Aerospace Eng. **22**, 15 (2009).

[8] J. Chen, A. Kitamura, E. Barbieri, D. Nishiura, and M. Furuichi, Analyzing effects of microscopic material parameters on macroscopic mechanical responses in underwater mixing using discrete element method, Powder Technol. **401**, 117304 (2022).

[9] H. Hertz, *Miscellaneous Papers* (Macmillan, New York, 1896).

[10] K. L. Johnson, K. Kendall, and A. D. Roberts, Surface energy and the contact of elastic solids, Proc. R. Soc. London, Ser. A **324**, 301 (1971).

[11] B. V. Derjaguin, V. M. Muller, and Y. P. Toporov, Effect of contact deformations on the adhesion of particles, J. Colloid Interface Sci. **53**, 314 (1975).

[12] C. K. Chan and C. L. Tien, Conductance of packed spheres in vacuum, J. Heat Transfer **95**, 302 (1973).

[13] C. Dominik and A. G. G. M. Tielens, The physics of dust coagulation and the structure of dust aggregates in space, Astrophys. J. **480**, 647 (1997).

[14] A. V. Gusarov, T. Laoui, L. Froyen, and V. I. Titov, Contact thermal conductivity of a powder bed in selective laser sintering, Int. J. Heat Mass Transf. **46**, 1103 (2003).

[15] N. Sakatani, K. Ogawa, Y. Iijima, M. Arakawa, R. Honda, and S. Tanaka, Thermal conductivity model for powdered materials under vacuum based on experimental studies, AIP Adv. **7**, 015310 (2017).

[16] S. Arakawa, H. Tanaka, A. Kataoka, and T. Nakamoto, Thermal conductivity of porous aggregates, Astron. Astrophys. **608**, L7 (2017).

[17] O. Ben-Nun, I. Einav, and A. Tordesillas, Force attractor in confined comminution of granular materials, Phys. Rev. Lett. **104**, 108001 (2010).

[18] R. Schräpler, J. Blum, I. von Borstel, and C. Güttler, The stratification of regolith on celestial objects, Icarus **257**, 33 (2015).

[19] F. Okubo and H. Katsuragi, Impact drag force exerted on a projectile penetrating into a hierarchical granular bed, Astron. Astrophys. **664**, A147 (2022).

[20] D. M. Mueth, H. M. Jaeger, and S. R. Nagel, Force distribution in a granular medium, Phys. Rev. E **57**, 3164 (1998).

[21] C. S. O'Hern, S. A. Langer, A. J. Liu, and S. R. Nagel, Force distributions near jamming and glass transitions, Phys. Rev. Lett. **86**, 111 (2001).

[22] T. S. Majmudar and R. P. Behringer, Contact force measurements and stress-induced anisotropy in granular materials, Nature (London) **435**, 1079 (2005).

[23] C. Güttler, M. Krause, R. J. Geretshauser, R. Speith, and J. Blum, The physics of protoplanetesimal dust agglomerates. IV. toward a dynamical collision model, Astrophys. J. **701**, 130 (2009).

[24] A. Kataoka, H. Tanaka, S. Okuzumi, and K. Wada, Static compression of porous dust aggregates, Astron. Astrophys. **554**, A4 (2013).

[25] T. Omura and A. M. Nakamura, Experimental study on compression property of regolith analogues, Planet. Space Sci. **149**, 14 (2017).

[26] S. Okuzumi, H. Tanaka, H. Kobayashi, and K. Wada, Rapid coagulation of porous dust aggregates outside the snow line: A pathway to successful icy planetesimal formation, Astrophys. J. **752**, 106 (2012).

[27] A. Kataoka, H. Tanaka, S. Okuzumi, and K. Wada, Fluffy dust forms icy planetesimals by static compression, Astron. Astrophys. **557**, L4 (2013).

[28] T. Okada, T. Fukuhara, S. Tanaka, M. Taguchi, T. Arai, H. Senshu, N. Sakatani, Y. Shimaki, H. Demura, Y. Ogawa, K. Suko, T. Sekiguchi, T. Kouyama, J. Takita, T. Matsunaga, T. Imamura, T. Wada, S. Hasegawa, J. Helbert, T. G. Müller *et al.*, Highly porous nature of a primitive asteroid revealed by thermal imaging, Nature (London) **579**, 518 (2020).

[29] H. Kobayashi and H. Tanaka, Rapid formation of gas-giant planets via collisional coagulation from dust grains to planetary cores, Astrophys. J. **922**, 16 (2021).

[30] R. Tazaki, C. Ginski, and C. Dominik, Fractal aggregates of submicron-sized grains in the young planet-forming disk around IM lup, Astrophys. J. Lett. **944**, L43 (2023).

[31] J. Blum, G. Wurm, S. Kempf, T. Poppe, H. Klahr, T. Kozasa, M. Rott, T. Henning, J. Dorschner, R. Schräpler, H. U. Keller, W. J. Markiewicz, I. Mann, B. A. S. Gustafson, F. Giovane, H. Fechtig *et al.*, Growth and form of planetary seedlings: Results from a microgravity aggregation experiment, Phys. Rev. Lett. **85**, 2426 (2000).

[32] D. Paszun and C. Dominik, The influence of grain rotation on the structure of dust aggregates, Icarus **182**, 274 (2006).

[33] T. Suyama, K. Wada, and H. Tanaka, Numerical simulation of density evolution of dust aggregates in protoplanetary disks. I. head-on collisions, Astrophys. J. **684**, 1310 (2008).

[34] P. Meakin, A historical introduction to computer models for fractal aggregates, J. Sol-Gel Sci. Technol. **15**, 97 (1999).

[35] J. Blum and G. Wurm, Experiments on sticking, restructuring, and fragmentation of preplanetary dust aggregates, Icarus **143**, 138 (2000).

[36] K. Wada, H. Tanaka, T. Suyama, H. Kimura, and T. Yamamoto, Numerical simulation of dust aggregate collisions. I. compression and disruption of two-dimensional aggregates, Astrophys. J. **661**, 320 (2007).

[37] M. Tatsuuma, A. Kataoka, and H. Tanaka, Tensile strength of porous dust aggregates, Astrophys. J. **874**, 159 (2019).

[38] M. Tatsuuma, A. Kataoka, S. Okuzumi, and H. Tanaka, Formulating compressive strength of dust aggregates from low to high volume filling factors with numerical simulations, Astrophys. J. **953**, 6 (2023).

[39] We note that an equivalent equation was derived in Ref. [51] in a smart way.

[40] H. Tanaka, K. Wada, T. Suyama, and S. Okuzumi, Growth of cosmic dust aggregates and reexamination of particle interaction models, Prog. Theor. Phys. Suppl. **195**, 101 (2012).

[41] S. Krijt, C. Güttler, D. Heißelmann, C. Dominik, and A. G. G. M. Tielens, Energy dissipation in head-on collisions of spheres, J. Phys. D **46**, 435303 (2013).

[42] S. Arakawa and S. Krijt, On the stickiness of CO_2 and H_2O ice particles, Astrophys. J. **910**, 130 (2021).

[43] Here we analyze all particle pairs with $x > 0$ as a postprocess analysis. Strictly speaking, two particles in contact do not detach at $x = 0$ but the contact breaks at $x = -(9/16)^{1/3}$ in the JKR model. However, in our compression simulation, the contribution of contacts with $x < 0$ should be negligibly small.

[44] S. Arakawa, M. Takemoto, and T. Nakamoto, Geometrical structure and thermal conductivity of dust aggregates formed via ballistic cluster-cluster aggregation, Prog. Theor. Exp. Phys. **2019**, 093E02 (2019).

[45] J. Haile, *Molecular Dynamics Simulation: Elementary Methods* (Wiley, New York, 1997).

[46] C. O'Sullivan, *Particulate Discrete Element Modelling: A Geomechanics Perspective* (CRC Press, Boca Raton, FL, 2011).

[47] S. Arakawa, M. Tatsuuma, N. Sakatani, and T. Nakamoto, Thermal conductivity and coordination number of compressed dust aggregates, Icarus **324**, 8 (2019).

[48] A. Seizinger and W. Kley, Bouncing behavior of microscopic dust aggregates, Astron. Astrophys. **551**, A65 (2013).

[49] C. Dominik and A. G. G. M. Tielens, Resistance to rolling in the adhesive contact of two elastic spheres, Philos. Mag., A **72**, 783 (1995).

[50] C. Dominik and A. G. G. M. Tielens, Resistance to sliding on atomic scales in the adhesive contact of two elastic spheres, Philos. Mag., A **73**, 1279 (1996).

[51] J. Chen, D. Krengel, D. Nishiura, M. Furuichi, and H.-G. Matuttis, A force displacement relation based on the JKR theory for DEM simulations of adhesive particles, Powder Technol. **427**, 118742 (2023).